www.nature.com/scientificreports

SCIENTIFIC REPORTS

OPEN

On the insulator-to-metal transition in titanium-implanted silicon

Fang Liu[1,2], Mao Wang[1,2], Yonder Berencén[1], Slawomir Prucnal[1], Martin Engler[1], René Hübner[1], Ye Yuan[1,2], René Heller[1], Roman Böttger[1], Lars Rebohle[1], Wolfgang Skorupa[1], Manfred Helm[1,2] & Shengqiang Zhou[1]

Received: 9 November 2017
Accepted: 23 February 2018
Published online: 07 March 2018

Hyperdoped silicon with deep level impurities has attracted much research interest due to its promising optical and electrical properties. In this work, single crystalline silicon supersaturated with titanium is fabricated by ion implantation followed by both pulsed laser melting and flash lamp annealing. The decrease of sheet resistance with increasing Ti concentration is attributed to a surface morphology effect due to the formation of cellular breakdown at the surface and the percolation conduction at high Ti concentration is responsible for the metallic-like conductivity. The insulator-to-metal transition does not happen. However, the doping effect of Ti incorporation at low concentration is not excluded, which might be responsible for the sub-bandgap optical absorption reported in literature.

Hyperdoping Si with deep level impurities is one of the most effective approaches to form an intermediate band (IB). IB materials are candidates for infrared photodetectors and highly efficient solar cells[1–8]. The strong optical absorption by transitions in the near-infrared range from 1100 to 2500 nm has been observed in S-, Se-, and Te-hyperdoped silicon[2,9,10]. Insulator-to-metal transition (IMT) has also been reported in S- and Se-hyperdoped silicon[6,11,12], which is a direct evidence for the formation of an IB. Titanium is another deep-level impurity candidate for forming an IB in Si[13–15]. Theoretical calculations predict that an IB can be formed in Si when Ti ions are at either interstitial or substitutional sites[6]. Indeed, Pastor *et al.* have shown that Ti impurities are located at interstitial lattice sites in Ti-hyperdoped Si fabricated by ion implantation and pulsed laser annealing[16]. On the other hand, Markevich *et al.* found evidences for the existence of substitutional Ti atoms in the Si lattice for samples implanted with Ti at very low fluences[17]. Nevertheless, Olea *et al.* observed a strong sub-bandgap absorption in Ti-implanted Si samples, suggesting the potential for optoelectronic applications[18,19]. Regarding the electrical properties of Ti-hyperdoped Si, it is believed that Ti behaves as a deep donor[20]. Several reports claim that with increasing Ti concentration a Mott-type insulator-to-metal transition occurs which is accompanied by the formation of an IB[14,15,20,21]. However, it is worth mentioning that the interface instability in form of a cellular breakdown[22,23] occurs when the Ti doping concentration reaches $1–2 \times 10^{21}$ cm^{-3} (2–4 at. %) during rapid solidification[24]. In a recent paper, we have also reported that the cellular breakdown takes place in Ti-implanted Si samples after pulsed laser annealing (PLA), but it can be effectively suppressed by millisecond-flash lamp annealing (FLA)[25]. The appearance of cellular breakdown prevents Ti incorporation into the single-crystalline Si matrix. Moreover, the inhomogeneous distribution of Ti impurities also complicates the interpretation of the electrical properties. Therefore, it still remains unclear whether the IMT in Ti-hyperdoped Si happens or not.

In the present work, Ti-hyperdoped Si is fabricated by ion implantation followed by PLA and FLA, respectively. We have investigated the structural and electrical properties in the fabricated Ti-hyperdoped Si samples. After FLA, the samples remain insulating even with the highest Ti implantation fluence, whereas the sheet resistance decreases with increasing Ti concentration after PLA. According to the results from conductive atomic force microscopy (C-AFM), the decrease of the sheet resistance after PLA is attributed to the percolation of Ti-rich cellular walls and not the insulator-to-metal transition due to Ti-doping.

Results

Recrystallization of Ti-implanted Si. Figure 1(a) and (b) show Raman spectra of Ti-implanted samples with fluences of 1.2×10^{16} cm^{-2} and 2×10^{15} cm^{-2} after PLA at an energy density of 0.8 J/cm^2 and after FLA at 55.5 J/cm^2, respectively. For comparison, the Raman spectra obtained from the as-implanted sample and the

[1]Helmholtz-Zentrum Dresden-Rossendorf, Institute of Ion Beam Physics and Materials Research, Bautzner Landstr. 400, 01328, Dresden, Germany. [2]Technische Universität Dresden, 01062, Dresden, Germany. Fang Liu and Mao Wang contributed equally to this work. Correspondence and requests for materials should be addressed to F.L. (email: f.liu@hzdr.de) or M.W. (email: m.wang@hzdr.de)

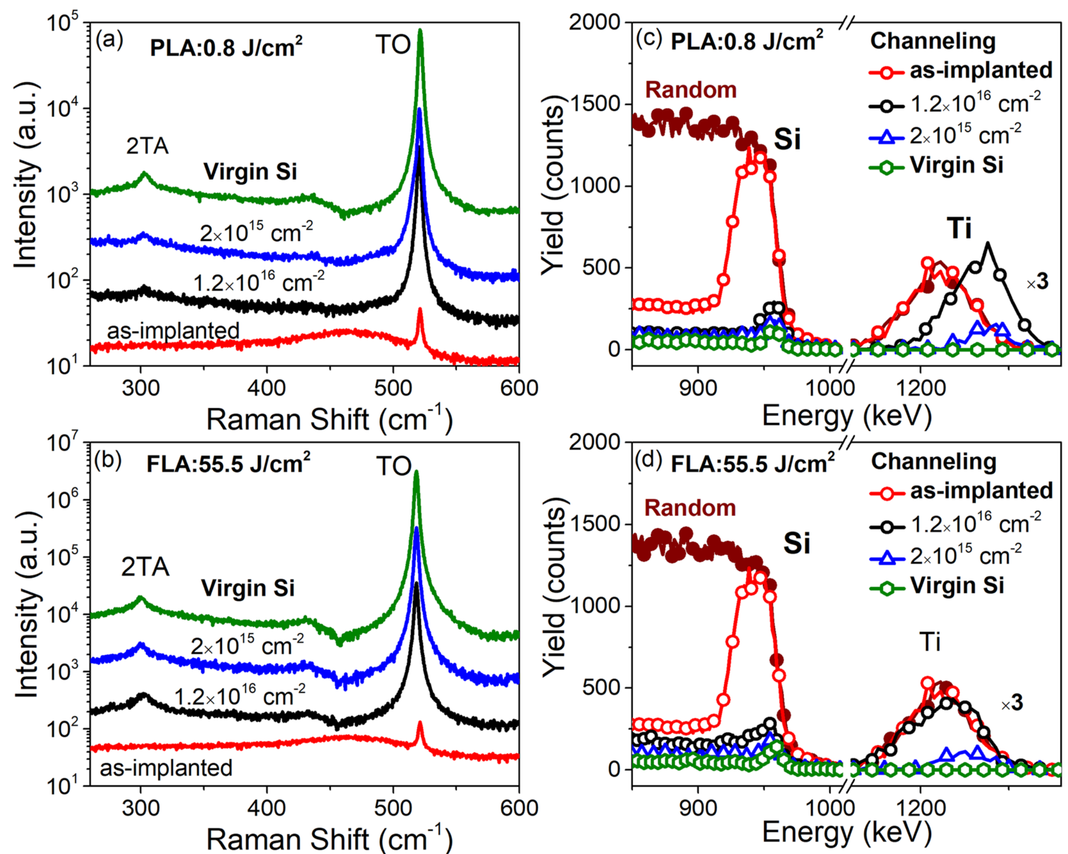

Figure 1. Raman scattering (**a**,**b**) and Rutherford backscattering spectrometry/channeling (cRBS) (**c**,**d**) spectra of Ti-implanted Si samples with fluences of $1.2 \times 10^{16}\,cm^{-2}$ and $2 \times 10^{15}\,cm^{-2}$ are shown in (**a**,**c**) after PLA at $0.8\,J/cm^2$ and (b, d) FLA at $55.5\,J/cm^2$. Both Raman and RBS spectra for virgin Si as well as the as-implanted samples with the fluence of $1.2 \times 10^{16}\,cm^{-2}$ are shown for comparison.

virgin Si are added. The Raman spectrum of virgin Si shows a narrow peak at around $520\,cm^{-1}$ which corresponds to the transverse optical (TO) phonon mode of single-crystalline Si. A weak band at around $460\,cm^{-1}$ is observed in the as-implanted sample due to amorphous layer formation upon ion implantation[26,27]. The weak peak at around $520\,cm^{-1}$ for the as-implanted sample is coming from the substrate which is not affected by the ion beam. After annealing, the band associated with the amorphous layer vanishes and the strong phonon mode at $520\,cm^{-1}$ corresponding to crystalline Si dominates the Raman spectra. The results prove that the crystal order, even in heavily implanted Si, can be well restored by both FLA and PLA.

RBS spectra obtained in both random and channeling configurations are shown in Fig. 1(c) and (d), respectively. The channeling minimum yield (χ_{min}) which measures the degree of lattice damage in the host semiconductor is defined as the ratio of the backscattering yield of the channeling and the random spectra. If the implanted layer is completely damaged after implantation, χ_{min} is 100%. On the contrary, a high-quality single crystal is expected to have a χ_{min} of around 1–2%. The as-implanted sample shows a broad damage peak at around 940 keV and its χ_{min} is calculated to be about 92%, showing that the implanted region becomes amorphous. After FLA or PLA, the backscattering yields in channeling condition are very close to that of the virgin Si, pointing out that the crystal order can be restored and thus a high-lattice quality is obtained. However, the channeling backscattering yield increases slightly with increasing ion fluence from $2 \times 10^{15}\,cm^{-2}$ to $1.2 \times 10^{16}\,cm^{-2}$ for both PLA and FLA samples. From the RBS results, the out-diffusion of Ti after PLA is clearly observed. As shown in Fig. 1(c), the Ti peak significantly shifts towards higher energies. The detailed results have been reported in ref.[25].

Lattice location of Ti impurities. To determine the location of the Ti atoms within the Si lattice, we show magnified RBS spectra corresponding to the Ti-related signal for the samples implanted with fluences of $2 \times 10^{15}\,cm^{-2}$ Fig. 2(a) and $1.2 \times 10^{16}\,cm^{-2}$ Fig. 2(b) being FLA-processed at $55\,J/cm^2$. As can be seen from these figures, there are no differences between the random and channeling RBS configuration for the Ti signal, indicating that most of the Ti atoms are not located at substitutional sites. In order to further investigate the position of the Ti atoms within Si, we performed angular scans about the [001] axis of Si. The normalized scattering yield for Si and Ti atoms at the same depth is plotted in Fig. 2(c). There are significant differences between the angular scans for Ti and Si. When the sample is tilted about Si [001], the channeling behavior for Si is clearly observed, but no change is detected for Ti. This indicates that Ti atoms are not located at the substitutional sites

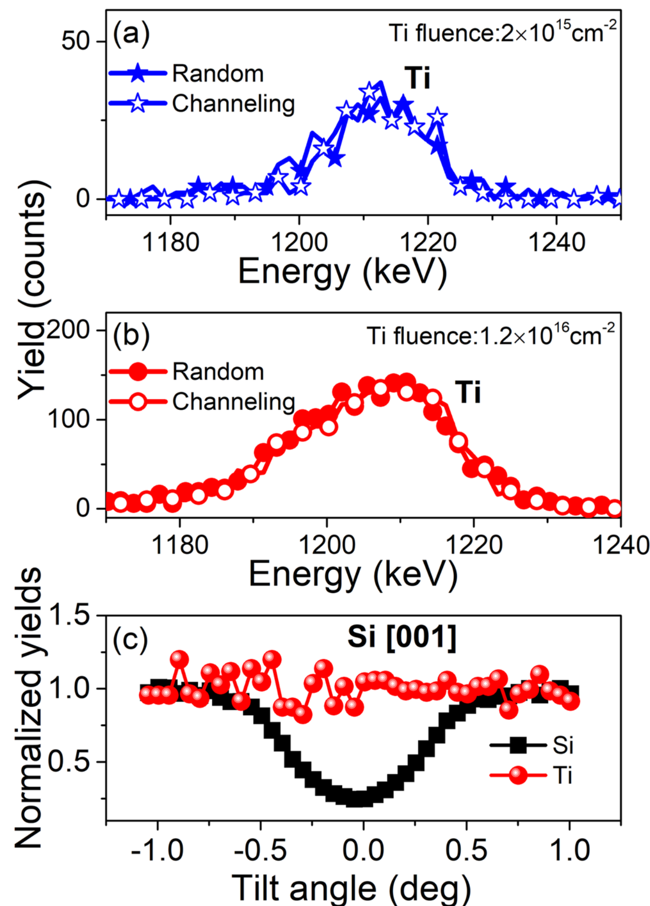

Figure 2. RBS spectra of Ti-implanted Si samples with fluences of 2×10^{15} cm^{-2} (**a**) and 1.2×10^{16} cm^{-2} (**b**) in random and channeling configuration for the Ti-related signal. Angular scans about the [001] direction for the Ti-implanted Si sample with a fluence of 1.2×10^{16} cm^{-2} (**c**). All samples shown here are flash lamp annealed.

based on the detection sensitivity of our technique[28,29]. According to cross-sectional TEM analysis, FLA leads to single-crystalline regrowth of the implanted region with the incorporation of defects, such as stacking faults. Additionally, hemispherical particles of single-crystalline nature, partially misaligned compared to the Si substrate and composed of Ti and Si are formed beneath the sample surface[25]. The RBS/channeling results can also be understood if the majority of the Ti atoms form polycrystalline secondary phases.

Electrical properties. Figure 3(a) shows the temperature-dependent sheet resistance over the temperature range 2.5–300 K for samples after different annealing conditions. The inset in Fig. 3(a) shows a linear scale representation of the sheet resistance as function of temperature for the sample PLA-1.2×10^{16} cm^{-2}. For the PLA samples, the sheet resistance decreases with increasing Ti doping. In case of samples with lower Ti concentration, the sheet resistance significantly increases with decreasing temperature, showing semiconducting behavior. However, the sheet resistance in samples with high Ti concentration shows only very weak temperature dependence [see the inset in Fig. 3(a)], similar to a metal with a low conductivity. The sheet resistance of the FLA-treated samples was found to be higher compared with the one measured in PLA-treated samples at the same implantation fluence of 1.2×10^{16} cm^{-2}. This suggests that the electrical conductivity of those samples has a different origin. Note that the as-implanted and the virgin samples are highly resistive with a sheet resistance larger than 10^6 Ω/sqr at room temperature.

As shown in Fig. 3(b), the temperature dependence of PLA samples can be scaled as:

$$R = R_0 exp\left(\frac{T_0}{T}\right)^{\frac{1}{2}} \tag{1}$$

where R_0 is a pre-exponential constant and T_0 is a characteristic temperature related with the material properties. The characteristic parameter T_0 extracted from the experimental data fitting was found to be 22.6 K (∼1.96 meV) and 1.9 K (∼0.16 meV) for the sample PLA-2×10^{15} cm^{-2} and the sample PLA-1.2×10^{16} cm^{-2}, respectively. This logarithmic scale of sheet resistance values as a function of $T^{-1/2}$ is characteristic of granular metals when transport is governed by tunneling among isolated metal grains[30–32], which refers to Ti cellular breakdown in the present case. Moreover, the magnitude of T_0 is greatly reduced with increasing Ti implantation fluences as seen

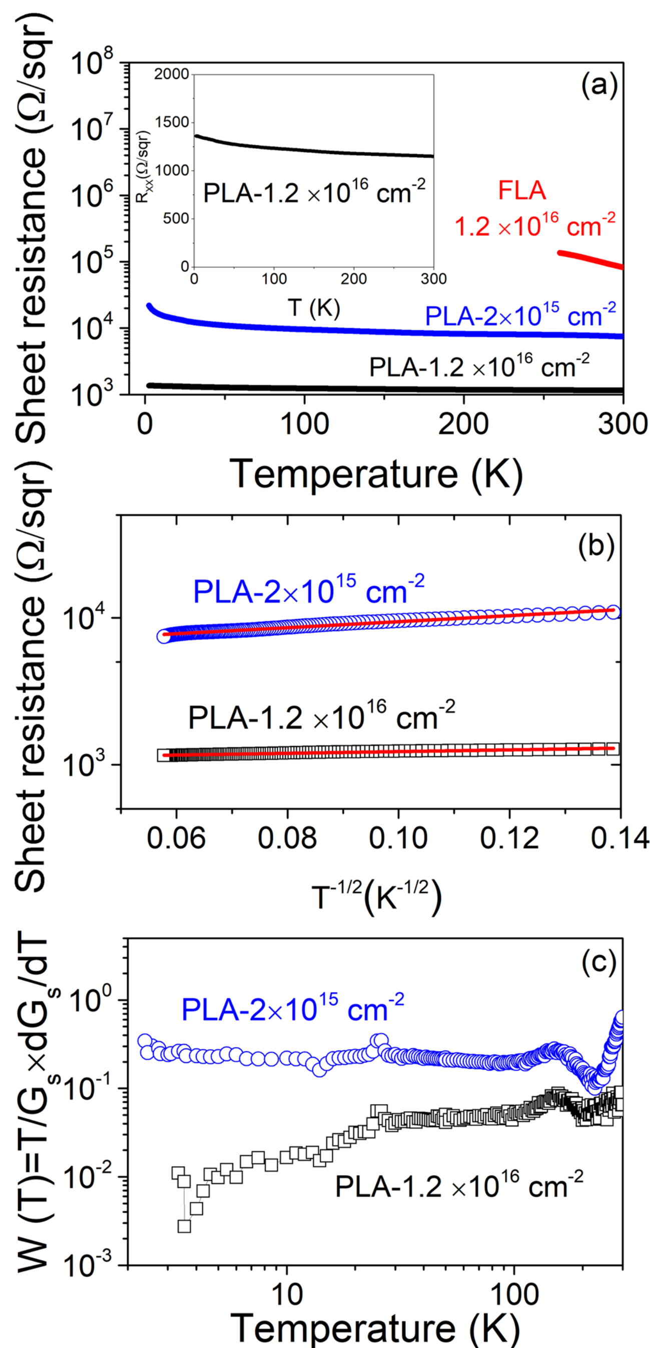

Figure 3. (**a**) Temperature-dependent sheet resistance of Ti-implanted Si after PLA and FLA. The inset shows the sheet resistance, in a linear scale, of the PLA-treated sample with a fluence of $1.2 \times 10^{16}\,cm^{-2}$. (**b**) Analysis of transport properties for PLA samples showing the sheet resistance values as a function of $T^{-1/2}$. (**c**) Reduced activation energy W of the conductance versus temperature for the PLA samples.

in Fig. 3(b). In comparison with the results reported in ref.[31], the sample PLA-$1.2 \times 10^{16}\,cm^{-2}$ lies at the percolation threshold. In addition, Fig. 3(c) shows the reduced activation energy of the conductance at various temperatures for the PLA samples, which is derived from the potential law[33] modelled as:

$$W = \frac{dlnG_s}{dlnT} = \left(\frac{T}{G_s}\right)\frac{dG_s}{dT} \tag{2}$$

where G_s is the sheet conductance deduced from the sheet resistance. As shown in Fig. 3(c), the reduced activation energy W is nearly zero for the sample PLA-$1.2 \times 10^{16}\,cm^{-2}$. This means that it exhibits a relatively finite conductivity as temperature tends to zero[34]. The decrease of W at low temperatures for the sample PLA-$1.2 \times 10^{16}\,cm^{-2}$ indicates that this sample lies in the metallic regime.

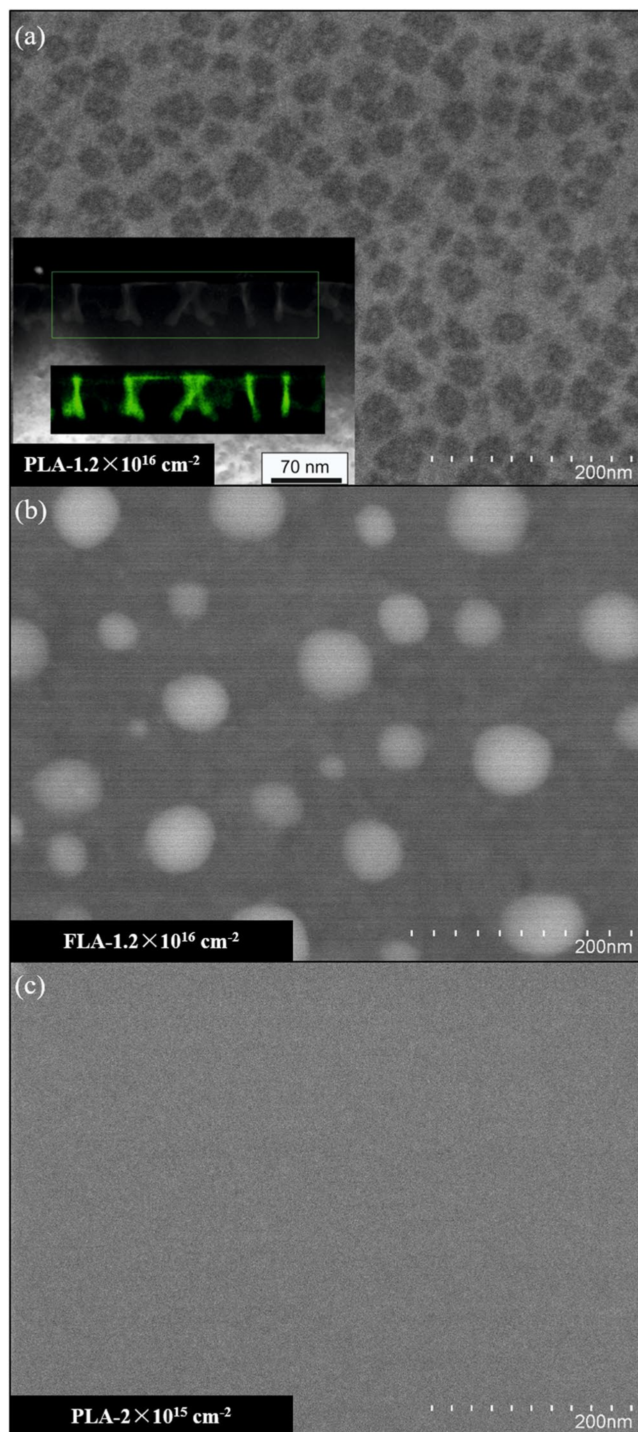

Figure 4. Top-view SEM image of the metallic sample PLA-1.2 × 10^{16} cm^{-2} (**a**), the insulating sample FLA-1.2 × 10^{16} cm^{-2} (**b**) and the insulating sample PLA-2 × 10^{15} cm^{-2} (**c**). The light-grey dots (sample FLA-1.2 × 10^{16} cm^{-2}) and nets (sample PLA-1.2 × 10^{16} cm^{-2}) are Ti-rich phases as identified by energy-dispersive X-ray spectroscopy. The inset in (**a**) displays a cross-sectional HAADF-STEM micrograph together with a Ti map (green color) obtained by energy-dispersive X-ray spectroscopy for the region marked by the green rectangle.

Surface morphology. Figure 4(a) shows a typical SEM micrograph of Ti-implanted Si with a fluence of 1.2 × 10^{16} cm^{-2} after PLA at 0.8 J/cm^2. Besides almost round dark-grey areas, light-grey regions are observed in the SEM micrograph. The inset in Fig. 4(a) shows the atomic-number contrast and the corresponding Ti map (green color) visualized by the high-angle annular dark-field scanning TEM (HAADF-STEM). The light-grey regions in the SEM micrograph belong to a Ti-rich cellular network structure. This network structure consists of (1) walls reaching from the sample surface to around 50 nm in depth and (2) a thin surface layer covering some of the cells formed by the walls mentioned above. According to high-resolution TEM analysis, the Ti-rich walls are characterized by an

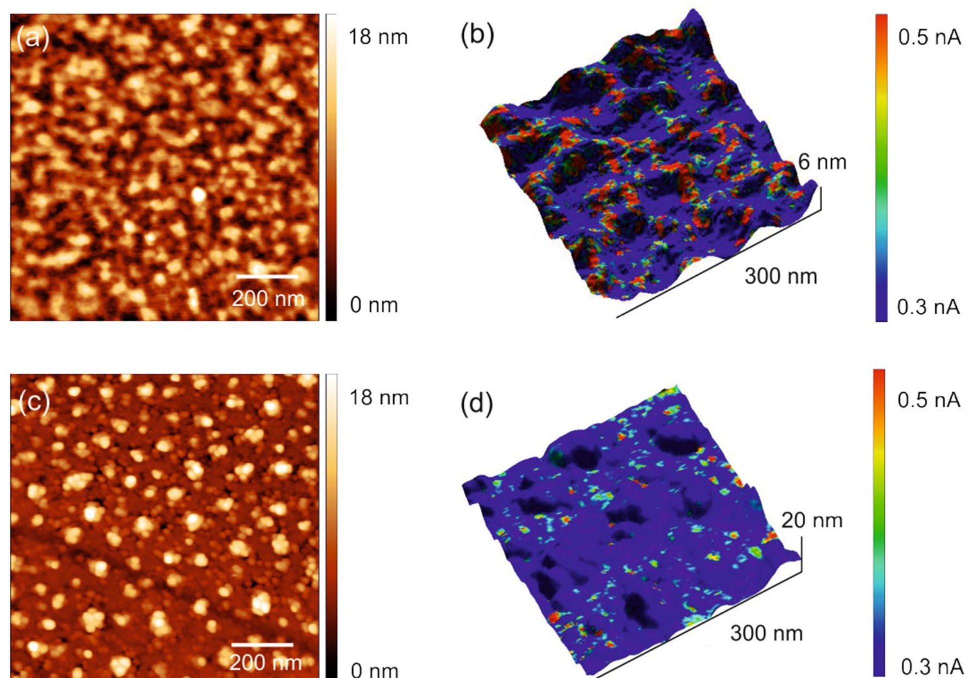

Figure 5. C-AFM analysis: (**a**,**c**) topography for the PLA/FLA samples, (**b**,**d**) overlay of current map and topography for the PLA/FLA samples. Both PLA and FLA sample are implanted with Ti at a fluence of 1.2×10^{16} cm^{-2}.

amorphous microstructure[25]. Hence, for the sample implanted at the highest fluence of 1.2×10^{16} cm^{-2}, a complete cellular breakdown occurs at the sample surface, which is due to the occurrence of constitutional supercooling in the molten stage[23,24,35]. At high enough impurity concentrations, a morphological instability occurs at the liquid-solid interface, resulting in the lateral segregation of Ti impurities and leading to a cellular solidification microstructure. In contrast, there is no cellular breakdown occurring for FLA-treated samples even at the highest Ti fluence as shown in Fig. 4(b). The light-grey dots correspond to a Ti-rich phase and are isolated from each other. For the sample PLA-2×10^{15} cm^{-2}, there is no detectable phase separation within the measurement sensitivity. Note that both FLA-1.2×10^{16} cm^{-2} and PLA-2×10^{15} cm^{-2} are insulating as shown in Fig. 3(a).

Spatially resolved conduction. The topographical images and the corresponding current maps of Ti-implanted Si samples with a fluence of 1.2×10^{16} cm^{-2} after PLA or FLA are shown in Fig. 5. The solidified cellular microstructure of the PLA sample can be observed in Fig. 5(a). The average cell size, determined to be ~65 nm, is slightly larger than the size obtained from TEM image (~50 nm)[25]. Instead of cellular microstructures, in Fig. 5(c), the topography of the sample after FLA shows bright spots corresponding to Ti-rich particles on the sample surface according to our TEM analysis[25]. Figure 5(b) and (d) show the overlay of current maps and topography, which provide the information about the local electrical properties of the surface layer. The current maps were measured with a sample bias voltage of +4 V. The significant dark blue areas imply current values of 0.3 nA or less. The current map shows cellular breakdown denoted as red spots in Fig. 5(b), pointing out that the electrical conductivity at the surface is not uniform. The red spots in the current map are almost connected with each other. The dark blue area shows an insulating background region. The current maps are well correlated with the topography for both samples. We can clearly observe that the conductive regions are mostly connected after PLA, whereas they are still isolated after FLA. We do believe that in Fig. 5(b) the conducting areas are associated with the cell structure formed during the rapid solidification process after PLA.

Discussion

For the PLA-treated samples, Ti diffuses towards the surface and form Ti-rich cell walls. In case of the FLA-treated samples, however, the out-diffusion of Ti is less pronounced (see Fig. 1) and hemispherical particles of single-crystalline nature containing Ti and Si are formed beneath the sample surface[25]. For those Ti impurities beneath the surface of the FLA samples, we deduced by using cRBS technique that the majority of the Ti impurities are neither located at the substitutional nor at the interstitial sites with high symmetry. This is actually in agreement with the quantum calculations based on density-functional theory[6]. Neither interstitial nor substitutional Ti implantation process is energetically favorable, however, interstitial Ti is less unstable by 0.65 eV. Experimentally however, we do not exclude the possibility of having Ti atoms located at the interstitial site with a low symmetry[29], i.e. Ti atoms are displaced from the symmetric interstitial site.

The change of the electrical transport properties shown in Fig. 3 may be due to the presence of percolation transition. A continuous conduction pathway spanning the sample's dimensions is initially formed at the threshold where the percolation takes place in conducting random networks. Therefore, our results exclude the presence

of a Mott-type insulator-to-metal transition in Ti-implanted Si. The metal-like conduction in samples after PLA is ascribed to the percolation of Ti-rich cell walls. Recently, atom probe tomography investigations on Co-implanted Si after PLA revealed that the phase separation does not lead to detectable silicides, but to a single-phase Si highly supersaturated with at least 10% atomic Co[36]. Moreover, our results do not exclude the fact that the infrared optical absorption reported in Ti implanted Si[18,19] likely comes from the region of Si doped with Ti at very low concentrations, which is far below the cellular breakdown threshold. Our qualitative analysis of the absorption properties by Fourier transform infrared spectroscopy (not shown) demonstrates a near- and mid- infrared optical absorption for both PLA and FLA samples. The measured optical absorption is comparable to that reported for Ti-implanted Si infrared photodetectors[37,38].

Conclusion

In summary, we have investigated the structural and electrical properties of Si implanted with Ti at very high concentrations followed by either PLA or FLA. We have demonstrated that the implanted samples are recrystallized after both PLA and FLA. C-AFM results exhibit conducting networks associated with cell structures which have been formed during the rapid solidification process during PLA. Temperature-dependent Hall effect measurements have revealed that the sheet resistance decreases with increasing Ti doping concentration for the PLA samples, which is in good agreement with the percolation transition. Our results exclude the occurrence of a Mott-type insulator-to-metal transition in Ti-implanted Si. However, the dilution of Ti ions into the Si matrix at very low concentrations is not discarded, which might be responsible for the infrared optical absorption.

Methods

Single-side polished, semi-insulating (100) Si wafers (resistivity $> 10^5\ \Omega\cdot$cm) with a thickness of 525 μm were implanted with Ti ions at an energy of 35 keV and fluences of $1.2 \times 10^{16}\,\mathrm{cm}^{-2}$, $6 \times 10^{15}\,\mathrm{cm}^{-2}$ and $2 \times 10^{15}\,\mathrm{cm}^{-2}$ at room temperature. In order to avoid channeling effects, samples were tilted by 7° with respect to the incident beam axis. The average thickness of the doped layer was about 60 nm[25]. After ion implantation, wafers were cut into pieces with a size of $5 \times 5\ \mathrm{mm}^2$. Two annealing methods, viz. millisecond-range FLA[39] for ms-range or PLA for ns-range were performed. The FLA was done in Ar ambient with an energy density in the range between 50 and 60 J/cm^2, corresponding to a surface temperature between 1100 and 1300 °C. A homogeneous flash was provided by the installed array of Xe-lamps connected in parallel with a reflector behind and a pre-heating module. The PLA was carried out in ambient using a XeCl excimer laser beam (Coherent COMPexPRO201, $\lambda = 308$ nm wavelengths, 28 ns pulse duration). A homogenized $5 \times 5\ \mathrm{mm}^2$ laser beam was produced with the help of a VarioLas optical system. During the PLA, a single laser pulse with an average energy density ranging from 0.2 to 0.8 J/cm^2 was applied to irradiate the as-implanted layers.

Raman spectroscopy was performed to investigate the crystalline quality of implanted and annealed samples. The Raman scattering spectra were obtained using a 532 nm Nd:YAG laser with a charge-coupled device camera cooled with liquid nitrogen. The crystallinity of the Si matrix after annealing and the location of the Ti impurities within the Si lattice were analyzed by channeling Rutherford backscattering spectrometry (cRBS). cRBS measurements were performed with a collimated 1.7 MeV He^+ beam at a 170° backscattering angle. The optimized energy densities for FLA and PLA were determined according to the structural properties after annealing, i.e. the narrowest Raman peak and the lowest channeling yield in RBS.

Electrical properties of implanted samples were examined using a commercial Lakeshore Hall System in van-der-Pauw-geometry between 2 and 300 K. The usage of a semi-insulating Si wafer makes the electrical measurements and data interpretation easier, since the parallel conductance from the thick insulating substrates can be neglected[20]. Scanning electron microscopy (SEM) using secondary electrons and backscattered electrons was applied to characterize the surface morphology and to qualitatively analyze the lateral compositional distribution, respectively. C-AFM was performed using tips with approx. 100 nm thick conductive diamond-like carbon coating to correlate the electrical conduction with the surface morphology.

References

1. Carey, J. E., Crouch, C. H., Shen, M. & Mazur, E. Visible and near-infrared responsivity of femtosecond-laser microstructured silicon photodiodes. *Opt. Lett* **30**, 1773–1775 (2005).
2. Said, A. J. *et al.* Extended infrared photoresponse and gain in chalcogen-supersaturated silicon photodiodes. *Appl. Phys. Lett* **99**, 073503 (2011).
3. Hu, S. *et al.* Improved photoresponse characteristics in Se-doped Si photodiodes fabricated using picosecond pulsed laser mixing. *Semicond. Sci. Technol* **27**, 102002 (2012).
4. Luque, A. & Martí, A. Increasing the efficiency of ideal solar cells by photon induced transitions at intermediate levels. *Phys. Rev. Lett* **78**, 5014 (1997).
5. Antolín, E. *et al.* Lifetime recovery in ultrahighly titanium-doped silicon for the implementation of an intermediate band material. *Appl. Phys. Lett* **94**, 042115 (2009).
6. Sánchez, K., Aguilera, I., Palacios, P. & Wahnón, P. Assessment through first-principles calculations of an intermediate-band photovoltaic material based on Ti-implanted silicon: Interstitial versus substitutional origin. *Phys. Rev. B* **79**, 165203 (2009).
7. Guenther, K.-M. *et al.* Excess carrier generation in femtosecond-laser processed sulfur doped silicon by means of sub-bandgap illumination. *Appl. Phys. Lett* **104**, 042107 (2014).
8. Berencén, Y. *et al.* Room-temperature short-wavelength infrared Si photodetector. *Sci. Rep* **7** (2017).
9. Crouch, C. H., Carey, J., Shen, M., Mazur, E. & Genin, F. Infrared absorption by sulfur-doped silicon formed by femtosecond laser irradiation. *Appl. Phys. A* **9**, 1635–1641 (2004).
10. Sheehy, M. A., Tull, B. R., Friend, C. M. & Mazur, E. Chalcogen doping of silicon via intense femtosecond-laser irradiation. *Mater. Sci. & Eng. B* **137**, 289–294 (2007).
11. Winkler, M. T. *et al.* Insulator-to-metal transition in sulfur-doped silicon. *Phys. Rev. Lett* **106**, 178701 (2011).
12. Ertekin, E. *et al.* Insulator-to-metal transition in selenium-hyperdoped silicon: observation and origin. *Phys. Rev. Lett* **108**, 026401 (2012).

13. Olea, J., Toledano-Luque, M., Pastor, D., González-Díaz, G. & Mártil, I. Titanium doped silicon layers with very high concentration. *J. Appl. Phys* **104**, 016105 (2008).
14. Pastor, D. *et al*. Insulator to metallic transition due to intermediate band formation in Ti-implanted silicon. *Sol. Energy Mater Sol. Cells* **104**, 159–164 (2012).
15. Castán, H. *et al*. Experimental verification of intermediate band formation on titanium-implanted silicon. *J. Appl. Phys* **113**, 024104 (2013).
16. Pastor, D. *et al*. Interstitial Ti for intermediate band formation in Ti-supersaturated silicon. *J. Appl. Phys* **112**, 113514 (2012).
17. Markevich, V. *et al*. Titanium in silicon: Lattice positions and electronic properties. *Appl. Phys. Lett* **104**, 152105 (2014).
18. Olea, J., Del Prado, A., Pastor, D., Mártil, I. & González-Díaz, G. Sub-bandgap absorption in Ti implanted Si over the Mott limit. *J. Appl. Phys* **109**, 113541 (2011).
19. Olea, J. *et al*. Room temperature photo-response of titanium supersaturated silicon at energies over the bandgap. *J. Phys. D: Appl. Phys*. **49**, 055103 (2016).
20. Olea, J., González-Díaz, G., Pastor, D. & Mártil, I. Electronic transport properties of Ti-impurity band in Si. *J. Phys. D: Appl. Phys*. **42**, 085110 (2009).
21. Zhou, Y., Liu, F., Zhu, M., Song, X. & Zhang, P. Insulator-to-metal transition in heavily Ti-doped silicon thin film. *Appl. Phys. Lett* **102**, 222106 (2013).
22. Narayan, J. Interface instability and cell formation in ion-implanted and laser-annealed silicon. *J. Appl. Phys* **52**, 1289–1293 (1981).
23. Recht, D. *et al*. Supersaturating silicon with transition metals by ion implantation and pulsed laser melting. *J. Appl. Phys* **114**, 124903 (2013).
24. Mathews, J. *et al*. On the limits to Ti incorporation into Si using pulsed laser melting. *Appl. Phys. Lett* **104**, 112102 (2014).
25. Liu, F. *et al*. Suppressing the cellular breakdown in silicon supersaturated with titanium. *J. Phys. D: Appl. Phys*. **49**, 245104 (2016).
26. Lee, M., Huang, C., Chang, Y. & Chao, Y. Double-resonance-enhanced Raman scattering in laser-recrystallized amorphous silicon film. *Phys. Rev. B* **40**, 10420 (1989).
27. Prucnal, S. *et al*. Formation of InAs quantum dots in silicon by sequential ion implantation and flash lamp annealing. *Appl. Phys. B* **101**, 315–319 (2010).
28. Swanson, M. Lattice location of solute atoms by channeling. *Vacuum* **39**, 87–90 (1989).
29. Jones, R., Öberg, S., Rasmussen, F. B. & Nielsen, B. B. Identification of the dominant nitrogen defect in silicon. *Phys. Rev. Lett* **72**, 1882 (1994).
30. Sheng, P., Abeles, B. & Arie, Y. Hopping conductivity in granular metals. *Phys. Rev. Lett* **31**, 44 (1973).
31. Abeles, B., Pinch, H. L. & Gittleman, J. I. Percolation conductivity in W-Al_2O_3 granular metal films. *Phys. Rev. Lett*. **35**(4), 247 (**1975**).
32. Shklovskii, B. I. & Efros, A. L. Electronic properties of doped semiconductors. *Springer Series in Solid-State Sciences* **45**, 203 (1984).
33. Zabrodskii, A. The Coulomb gap: the view of an experimenter. *Philos. Mag. B*. **81**, 1131–1151 (2001).
34. García-Hemme, E. *et al*. Insulator-to-metal transition in vanadium supersaturated silicon: variable-range hopping and Kondo effect signatures. *J. Phys. D: Appl. Phys* **49**, 275103 (2016).
35. Cullis, A. *et al*. Growth interface breakdown during laser recrystallization from the melt. *Appl. Phys. Lett* **38**, 642–644 (1981).
36. Akey, A. J., Recht, D., Williams, J. S., Aziz, M. J. & Buonassisi, T. Single-Phase Filamentary Cellular Breakdown Via Laser-Induced Solute Segregation. *Adv. Funct. Mater* **25**, 4642–4649 (2015).
37. García-Hemme, E. *et al*. Sub-bandgap spectral photo-response analysis of Ti supersaturated Si. *Appl. Phys. Lett* **101**, 192101 (2012).
38. García-Hemme, E. *et al*. Room-temperature operation of a titanium supersaturated silicon-based infrared photodetector. *Appl. Phys. Lett* **104**, 211105 (2014).
39. Skorupa, W. *et al*. Advanced thermal processing of ultrashallow implanted junctions using flash lamp annealing. *J. Electrochem. Soc* **152**, G436–G440 (2005).

Acknowledgements

Support by the Ion Beam Center (IBC) at HZDR is gratefully acknowledged. This work was supported by the Helmholtz-Gemeinschaft Deutscher Forschungszentren (HGF-VH-NG-713). F.L. and M.W. would like to thank the financial support by the China Scholarship Council (File No. 201307040037 and No. 201506240060, respectively). Y.B. would like to thank the Alexander-von-Humboldt foundation for providing a postdoctoral fellowship.

Author Contributions

F.L. and M.W. designed the research work and wrote the manuscript. F.L. and Y.B. performed the Raman structural experiments. S.P. performed the flash-lamp annealing. F.L. and R. Heller did the RBS measurements. M.W. carried out the transport measurements and performed the electrical properties analysis. M.E. carried out the C-AFM experiments, while Y.Y. and L.R. contributed to the physical understanding. R. Hübner conducted the TEM and SEM measurements together with the data analysis. R.B. did the high-fluence Ti implantation. W.S., M.H. and S.Z. supervised the research and provided the required support. All authors contributed to the discussion and correction of the manuscript.

Additional Information

Competing Interests: The authors declare no competing interests.

Publisher's note: Springer Nature remains neutral with regard to jurisdictional claims in published maps and institutional affiliations.

Open Access This article is licensed under a Creative Commons Attribution 4.0 International License, which permits use, sharing, adaptation, distribution and reproduction in any medium or format, as long as you give appropriate credit to the original author(s) and the source, provide a link to the Creative Commons license, and indicate if changes were made. The images or other third party material in this article are included in the article's Creative Commons license, unless indicated otherwise in a credit line to the material. If material is not included in the article's Creative Commons license and your intended use is not permitted by statutory regulation or exceeds the permitted use, you will need to obtain permission directly from the copyright holder. To view a copy of this license, visit http://creativecommons.org/licenses/by/4.0/.

© The Author(s) 2018